# **ChemComm**



## COMMUNICATION

View Journal



Cite this: DOI: 10.1039/d5cc03833b

Received 7th July 2025, Accepted 3rd October 2025

DOI: 10.1039/d5cc03833b

rsc.li/chemcomm

# A Ta<sub>3</sub>N<sub>5</sub>/BN composite for enhanced photocatalytic water splitting

Yao Xu, Haifeng Wang, Jiaming Zhang, Zihao Zhang, Meng Liu, Xiaowei Tao, Jifang Zhang\* and Guijun Ma \*\*D\*\*

Narrow-bandgap  $Ta_3N_5$  nanorods were supported on a BN substrate to produce a composite photocatalyst using  $NH_4Cl$ -based vacuum nitridation. The charge separation efficiency of  $Ta_3N_5$  was effectively enhanced due to electron transfer from  $Ta_3N_5$  to the BN substrate, boosting both the photocatalytic water oxidation and Z-scheme overall water splitting reactions.

Solar energy conversion into clean hydrogen resources through a photocatalytic process is a promising strategy for sustainable energy systems. 1,2 However, the development of efficient photocatalysts is constrained by limitations in light harvesting, especially in the visible region that makes up 45% of the solar spectrum,<sup>3</sup> and photon conversion efficiency, restrained by serious bulk and surface charge recombinations. 4-8 Ta<sub>3</sub>N<sub>5</sub> has emerged as a particularly promising photocatalyst due to its bandgap of only 2.1 eV. The conduct band minimum (CBM) and valence band maximum (VBM) of Ta<sub>3</sub>N<sub>5</sub> are composed of Ta 5d and N 2p orbitals, respectively, thermodynamically allowing for both photocatalytic and photoelectrochemical water redox reactions.<sup>9,10</sup> In 2002, Hitoki et al. reported photocatalytic water oxidation on Ta<sub>3</sub>N<sub>5</sub> in the presence of an electron acceptor.11 However, subsequent studies have demonstrated that the performance of Ta<sub>3</sub>N<sub>5</sub> is fundamentally limited by issues directly stemming from the synthesis method. Specifically, Ta<sub>3</sub>N<sub>5</sub> is typically prepared through an NH<sub>3</sub>-based thermal nitridation process, which meets challenges including the formation of low-valence metal ions and  $O_N$  anti-site defects within the crystal structure. These intrinsic defects act as recombination centers that severely suppress the charge separation efficiency. 12,13 Furthermore, high temperature duration leads to particle agglomeration of the products, exacerbating charge recombination issues. As a consequence of these synthesis-related challenges, Ta<sub>3</sub>N<sub>5</sub> exhibits unsatisfactory photon conversion efficiencies in photocatalytic reactions. 14-16

School of Physical Science and Technology, ShanghaiTech University, Shanghai 201210, China. E-mail: zhangjf3@shanghaitech.edu.cn, magj@shanghaitech.edu.cn

Nanostructural engineering, by precisely controlling the morphology and architecture of oxide precursors, has emerged as an effective strategy to improve the charge separation efficiency in Ta<sub>3</sub>N<sub>5</sub> photocatalysts by reducing the charge transport distances and extending the carrier lifetimes. 17 Ma et al. applied a Ta<sub>2</sub>O<sub>5</sub> and Na<sub>2</sub>CO<sub>3</sub> mixture to produce a NaTaO<sub>3</sub>/Ta<sub>2</sub>O<sub>5</sub> composite, which was then used as a precursor for thermal ammonolysis. This method suppressed Ta<sub>3</sub>N<sub>5</sub> agglomeration and enhanced the crystallinity.14 Wang et al. prepared Ta<sub>2</sub>O<sub>5</sub>-coated Pt/SiO<sub>2</sub> nanoparticles for the fabrication of hollow Ta<sub>3</sub>N<sub>5</sub> nanoshells, and subsequently loaded CoO<sub>x</sub> onto the outer surface of Ta<sub>3</sub>N<sub>5</sub> with Pt left on the inner shell after removing SiO2.18 The nanoshell structure not only provided a structural framework for efficient charge transport but also facilitated directional carrier extraction by spatially separating the reduction and oxidation cocatalysts, thus boosting charge separation. Wang et al. applied KTaO<sub>3</sub> as a vaporous Ta resource to produce Ta3N5 nanorod single crystals and accelerate heating of the ammonium flow, which reduced the duration of the nitridation process. The highly crystallized Ta<sub>3</sub>N<sub>5</sub> nanorods with fewer defects realized one-step excitation in the overall water splitting reaction under visible light illumination.9 Nanostructured precursors enable controlled Ta<sub>3</sub>N<sub>5</sub> particle morphology, effectively decreasing agglomeration and shortening the carrier transport distances, while structuring the catalyst/host interface promotes more efficient carrier transport, enhancing the charge separation efficiency and thereby unlocking Ta<sub>3</sub>N<sub>5</sub>'s potential for photocatalysis.

Our group has developed a  $NH_4Cl$ -based vacuum nitridation method to synthesize transition metal (oxy)nitrides such as a  $Ta_3N_5/Ta$  thin film,  $^{19}$  TaON powders $^{20}$  and ZnO:GaN nanoparticles.  $^{21,22}$  For the preparation of the  $Ta_3N_5/Ta$  thin film, only a Ta wafer and  $NH_4Cl$  were used as precursors. Upon heating, in the first step,  $NH_3$  and HCl are produced from the decomposition of  $NH_4Cl$ . The metallic Ta reacts with HCl to produce a gaseous  $TaCl_5$  intermediate, which subsequently reacts with  $NH_3$  to form  $Ta_3N_5$  particles on the surface of the Ta plate. The high permeability of the gaseous  $TaCl_5$  and  $NH_3$ 

Communication ChemComm

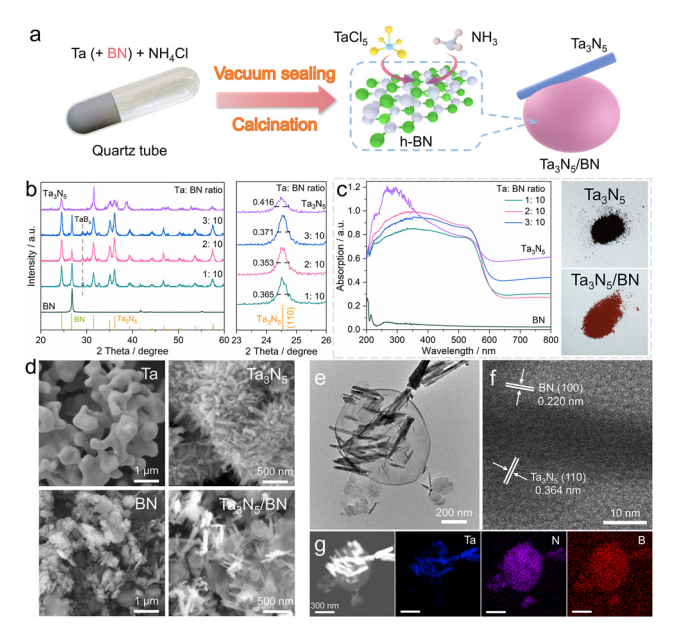


Fig. 1 (a) Illustration of the synthesis of the  $Ta_3N_5/BN$  composite. (b) XRD patterns of the BN precursor, bulk Ta<sub>3</sub>N<sub>5</sub>, and Ta<sub>3</sub>N<sub>5</sub>/BN samples prepared from different Ta/BN ratios. (c) UV-vis DRS of the BN, Ta<sub>3</sub>N<sub>5</sub>, and Ta<sub>3</sub>N<sub>5</sub>/BN powders, as well as digital images of the  $Ta_3N_5$  and  $Ta_3N_5/BN$  (Ta:BN =2:10) samples. (d) SEM images of the Ta and BN precursors and corresponding  $Ta_3N_5$  and  $Ta_3N_5/BN$  products. (e) TEM, (f) HRTEM, and (g) dark field image and EDS mapping images of the  $Ta_3N_5/BN$  (Ta:BN = 2:10) sample. The referenced patterns of BN and  $Ta_3N_5$  in (b) are ICDD-00-045-1171 and ICDD-04-004-4564, respectively.

reactants not only leads to rapid crystallization of the solid product but also prevents Ta<sub>3</sub>N<sub>5</sub> from forming reduced Ta species by limiting exposure to an NH<sub>3</sub> atmosphere.

Herein, we introduce two-dimensional BN as a substrate for the growth of Ta<sub>3</sub>N<sub>5</sub> nanoparticles in an NH<sub>4</sub>Cl-based nitridation process. The involvement of BN in the precursor led to improved crystallinity and dispersion of the Ta<sub>3</sub>N<sub>5</sub> particles. Reductive photodeposition of Ag and Rh suggested that electrons were transferred from Ta<sub>3</sub>N<sub>5</sub> to BN under irradiation. Such directional charge migration greatly enhanced the photocatalytic activity of Ta<sub>3</sub>N<sub>5</sub> for water splitting, highlighting the benefits of photocatalyst-substrate interaction.

The Ta<sub>3</sub>N<sub>5</sub> bulk and Ta<sub>3</sub>N<sub>5</sub>/BN composite were synthesized by vacuum sealing a mixture of NH<sub>4</sub>Cl and metallic Ta powder in a quartz tube with or without adding BN (Fig. 1a, with details shown in the SI). For Ta<sub>3</sub>N<sub>5</sub>/BN, the atomic ratios of Ta:BN were set as 1:10, 2:10 and 3:10, respectively. Fig. 1b displays the X-ray diffraction (XRD) patterns of the powders prepared with different Ta:BN ratios. All the BN-containing samples exhibit patterns of mixed BN and Ta<sub>3</sub>N<sub>5</sub> peaks, with a weak signal at  $\sim 29^{\circ}$  assigned to TaB<sub>x</sub> impurities. The majority of the peaks of Ta<sub>3</sub>N<sub>5</sub>/BN are consistent with the standard Ta<sub>3</sub>N<sub>5</sub> patterns, indicating the high purity of Ta<sub>3</sub>N<sub>5</sub> in the obtained samples. No signals of metallic Ta are observed in the products. Additionally, the full-width half-maximum (FWHM) of the Ta<sub>3</sub>N<sub>5</sub> (110) diffraction peaks in the Ta<sub>3</sub>N<sub>5</sub>/BN samples is lower than that of Ta<sub>3</sub>N<sub>5</sub>, indicating enhanced crystallinity of Ta<sub>3</sub>N<sub>5</sub>

when BN is present during synthesis. Fig. 1c shows the UV-vis diffuse reflectance spectroscopy (DRS) of the BN, Ta<sub>3</sub>N<sub>5</sub> and Ta<sub>3</sub>N<sub>5</sub>/BN powders. The BN precursor exhibits negligible UVvisible light absorption due to its wide bandgap of 5.1 eV. The Ta<sub>3</sub>N<sub>5</sub> reference powder shows a broad absorption up to 600 nm corresponding to its bandgap (2.1 eV). The observed dark brown color, as opposed to dark red, can be attributed to elevated absorption in the near-infrared region. All of the Ta<sub>3</sub>N<sub>5</sub>/BN samples exhibit smooth band-to-band absorption features typical of Ta<sub>3</sub>N<sub>5</sub>, revealing that the optical properties of Ta<sub>3</sub>N<sub>5</sub> did not change with the introduction of BN into the precursor, as corroborated by the Tauc plots in Fig. S1. Compared to Ta<sub>3</sub>N<sub>5</sub>, the relatively lower background levels above 600 nm for the Ta<sub>3</sub>N<sub>5</sub>/BN samples suggest less absorption associated with intragap defect states. Notably, the Ta:BN = 2:10 sample achieves the strongest light absorption, showing that photon absorption does not linearly increase with a higher Ta ratio in the precursor.

The scanning electron microscopy (SEM) images (Fig. 1d) display the morphology of the precursors and the nitridation products. Without incorporating BN during nitridation, large Ta precursor particles are converted into aggregated Ta<sub>3</sub>N<sub>5</sub> nanorods. In the presence of BN, the nitridation products show more uniformly distributed and well-isolated Ta<sub>3</sub>N<sub>5</sub> particles dispersed on the BN substrate. The SEM images of the different Ta<sub>3</sub>N<sub>5</sub>/BN samples (Fig. S2) in back scattered electron (BSE) mode show that the dispersity of the Ta<sub>3</sub>N<sub>5</sub> nanorods in the Ta:BN = 2:10 sample is higher than that in the 1:10 and 3:10 samples. This demonstrates that the Ta content effectively impacts the growth of Ta<sub>3</sub>N<sub>5</sub> particles, highlighting NH<sub>4</sub>Clbased vacuum nitridation as a potential method for constructing regulated nanostructures. The transmission electron microscopy (TEM) image of the Ta:BN = 2:10 sample (Fig. 1e) shows  $Ta_3N_5$ nanorods with lengths around hundreds of nanometers lying on the BN substrate. The BN structure remains unchanged after the high-temperature nitridation. The TEM image clearly demonstrates that the Ta<sub>3</sub>N<sub>5</sub> particles in the obtained samples adopt a typical nanorod morphology, which is similar to the Ta<sub>3</sub>N<sub>5</sub> particles prepared directly from TaCl<sub>5</sub> and NH<sub>3</sub> precursors.<sup>23</sup> The high-resolution TEM (HRTEM) image in Fig. 1f exhibits the interface of the Ta<sub>3</sub>N<sub>5</sub> and BN particles. The close stacking of the 0.364 nm lattice fringes assigned to the (110) facet of Ta<sub>3</sub>N<sub>5</sub> and the 0.220 nm lattice fringes assigned to the BN (100) facet suggests the growth of Ta<sub>3</sub>N<sub>5</sub> on the BN substrate. Fig. 1g shows the TEM dark field image and energy dispersive X-ray spectroscopy (EDS) of the Ta:BN = 2:10 sample. The overlapped N and Ta signals further confirm the nanorod morphology of Ta<sub>3</sub>N<sub>5</sub> on the BN substrate.

XPS analysis was carried out on the  $Ta_3N_5$ , BN and  $Ta_3N_5/BN$ particles. The well-defined double peaks at 25.2 and 27.1 eV (Fig. 2a) assigned to Ta  $4f_{7/2}$  and  $4f_{5/2}$  in Ta<sub>3</sub>N<sub>5</sub> reveal that the NH<sub>4</sub>Cl-based nitridation suppresses the formation of reduced Ta species. For the Ta<sub>3</sub>N<sub>5</sub>/BN particles, additional double peaks are observed at high field shift, which are supposed to be TaO<sub>r</sub> impurities.<sup>24</sup> The O 1s spectrum (Fig. S3) reveals the existence of crystalline O species in Ta<sub>3</sub>N<sub>5</sub> and Ta<sub>3</sub>N<sub>5</sub>/BN, suggesting

ChemComm

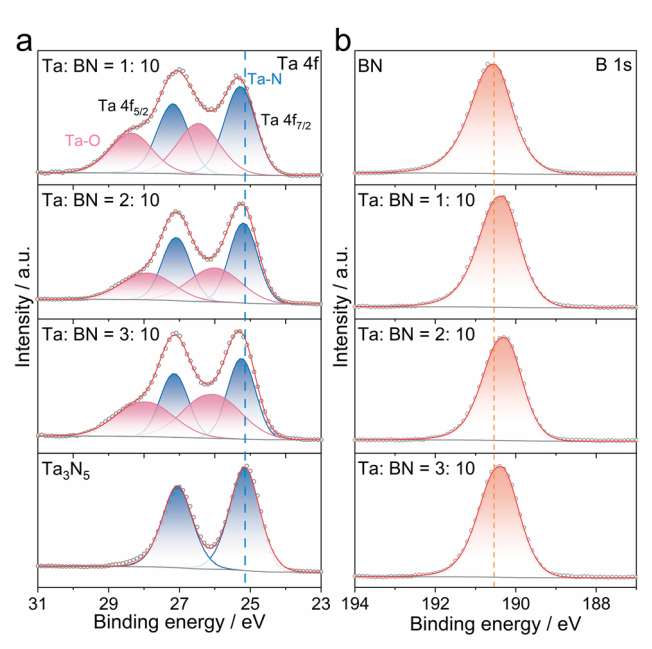


Fig. 2 XPS of the  $Ta_3N_5/BN$  samples prepared from different precursor ratios, including  $Ta_3N_5$  and BN for reference. (a) Ta 4f and (b) B 1s spectra.

surface coverage of the  ${\rm TaO}_x$  species. Besides, compared with  ${\rm Ta}_3{\rm N}_5$ , a slightly higher binding energy of the  ${\rm Ta}^{5+}$  signals in  ${\rm Ta-N}$  of the  ${\rm Ta}_3{\rm N}_5/{\rm BN}$  samples reflects a possible electron transfer from  ${\rm Ta}_3{\rm N}_5$  to BN. Relative to BN, the lower shift in B 1s binding energy for the  ${\rm Ta}_3{\rm N}_5/{\rm BN}$  samples also suggests an interfacial electron transfer between the two components (Fig. 2b).

To verify electron transfer between Ta<sub>3</sub>N<sub>5</sub> and BN under illumination, visible light-driven photoreduction of Ag<sup>+</sup> ions was performed, and Ag particles were loaded on the Ta<sub>3</sub>N<sub>5</sub>/BN composite photocatalyst. The 0.200 nm lattice fringes attributed to the Ag (103) facet are observed on both the BN and Ta<sub>3</sub>N<sub>5</sub> particles. The EDS mappings in Fig. 3c clearly distinguish the Ag nanoparticles loaded away from the Ta<sub>3</sub>N<sub>5</sub> nanorods. Considering that BN barely absorbs visible light, this indicates that photogenerated electrons are partially transferred from Ta<sub>3</sub>N<sub>5</sub> to BN, as illustrated in the structure diagram of Fig. 3c. As further evidence, by using Rh<sup>3+</sup> as a precursor, Rh nanoparticles can also be reductively photodeposited on the BN substrate (Fig. S4). Mott-Schottky analysis and valence spectra (Fig. S5) reveal that the Fermi level of BN is closely aligned with that of Ta<sub>3</sub>N<sub>5</sub>. Such energetic alignment is beneficial for electron transfer from Ta<sub>3</sub>N<sub>5</sub> to BN.

Transient absorption spectroscopy was employed to investigate the electron transfer from  $Ta_3N_5$  to BN under light excitation and in solution. The pump and probe lights were set at 355 and 580 nm, respectively. For BN alone (Fig. S6), no meaningful transient absorption signal is observed as its band gap exceeds the pump light wavelength. In contrast, both  $Ta_3N_5$  and  $Ta_3N_5/8N$  show a weak negative absorption at 580 nm (Fig. 3d). To assign this signal, L-ascorbic acid is added as a hole scavenger. Here, the intensity of the negative absorption increases for both samples, confirming that this signal is associated with

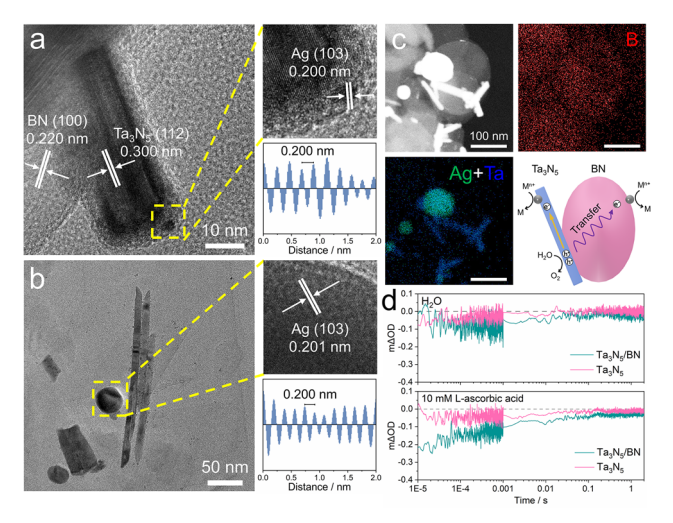


Fig. 3 HRTEM images and lattice fringe distances of the Ag particles loaded on (a)  $Ta_3N_5$  and (b) BN in the  $Ta_3N_5/BN$  particles. (c) Dark field image, EDS mappings and structure diagram of the  $Ta_3N_5/BN$  sample loaded with Ag. (d) Transient absorption spectrum for  $Ta_3N_5$  and  $Ta_3N_5/BN$  in water without (top panel) or with L-ascorbic acid (bottom panel). The pump and probe lights in (d) are 355 and 580 nm, respectively. The  $Ta_3N_5/BN$  sample is prepared from a Ta:BN=2:10 ratio.

photogenerated electrons. It is worth noting that the negative absorption for  $Ta_3N_5/BN$  is significantly stronger than that for  $Ta_3N_5$ , indicating superior charge carrier separation in the former sample.

The catalyst–substrate electron transfer in  $Ta_3N_5/BN$  is supposed to promote its photocatalytic performance *via* improving electron–hole separation. Fig. 4a displays the activities of the photocatalytic oxygen evolution reaction (OER) on  $Ta_3N_5$  or

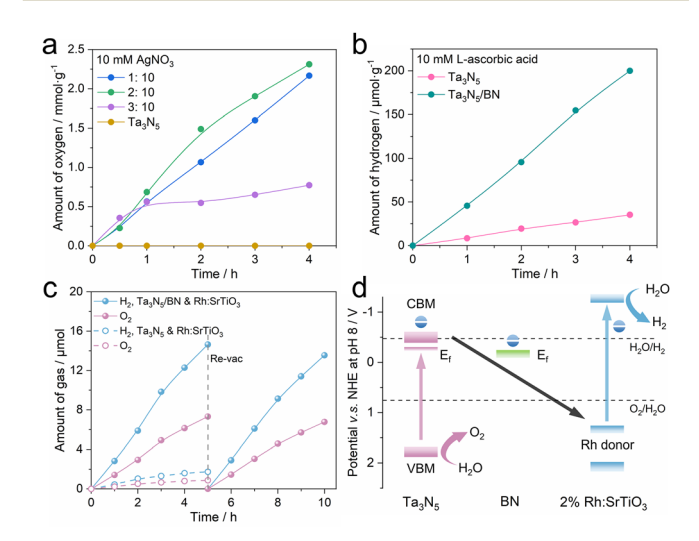


Fig. 4 (a) Time profiles of photocatalytic OER on  $Ta_3N_5/BN$  and bulk  $Ta_3N_5$  samples in  $AgNO_3$  reagent. (b) HER activities of  $Ta_3N_5/BN$  and  $Ta_3N_5$  in L-ascorbic acid reagent. (c)  $H_2$  and  $O_2$  production from physical oscillation between  $Ta_3N_5/BN$  and 2% Rh:SrTiO $_3$  at pH 5. (d) Diagram of Z-scheme electron transfer between  $Ta_3N_5/BN$  and Rh:SrTiO $_3$ . The  $Ta_3N_5/BN$  in (b) and (c) are prepared from a Ta:BN=2:10 ratio and each assessment applied 30 mg of catalyst. 0.75 wt%  $IrO_2$  and 1 wt% Pt were loaded as cocatalysts for OER and HER, respectively.

Communication ChemComm

Ta<sub>3</sub>N<sub>5</sub>/BN in the presence of AgNO<sub>3</sub> as an electron scavenger. An IrO<sub>2</sub> species is loaded on the catalysts to assist the OER process (Fig. S7). The Ta<sub>3</sub>N<sub>5</sub> nanorods barely produce oxygen due to rapid passivation by Ag coverage on their active sites.<sup>23</sup> However, Ta<sub>3</sub>N<sub>5</sub>/BN exhibits linear oxygen evolution in the early stages, revealing that electron interaction slows down the Ag passivation and preserves the photocatalytic activity. Among the  $Ta_3N_5/BN$  products, the Ta:BN = 2:10 sample has the highest water oxidation rate. This is likely due to better photon absorption (Fig. 1c) and the more uniform distribution of Ta<sub>3</sub>N<sub>5</sub> nanorods on the BN substrate (Fig. S2) for this sample.

Fig. 4b displays photocatalytic hydrogen evolution (HER) on  $Ta_3N_5/BN$  (Ta:BN = 2:10) and  $Ta_3N_5$  assisted with L-ascorbic acid as a hole sacrificial reagent. Pt (1 wt%) is optimized as the HER cocatalyst (Fig. S7). The Ta<sub>3</sub>N<sub>5</sub>/BN composite structure also shows a considerably enhanced hydrogen evolution rate compared with Ta<sub>3</sub>N<sub>5</sub> nanorods, although it remains much lower than the OER rate. This highlights the thermodynamic limitations of Ta<sub>3</sub>N<sub>5</sub>/BN for proton reduction (Fig. S8). To break such limitations, Fig. 4c displays a Z-scheme overall water splitting reaction by physical collision between Ta<sub>3</sub>N<sub>5</sub>/BN and Rh-doped SrTiO<sub>3</sub> (Rh:SrTiO<sub>3</sub>) particles. Under visible light illumination, stoichiometric hydrogen and oxygen evolution over 10 h is realized for Ta<sub>3</sub>N<sub>5</sub>/BN, while the Ta<sub>3</sub>N<sub>5</sub> exhibits significantly lower activity. Fig. 4d represents the band structure of Ta<sub>3</sub>N<sub>5</sub>/BN and Rh:SrTiO<sub>3</sub> determined from Mott-Schottky and bandgap assessment in Fig. S9. It is obvious that transfer of photogenerated electrons from Ta<sub>3</sub>N<sub>5</sub> to BN favors the Z-scheme electron transfer pathway, effectively overcoming the insufficient reduction driving force of Ta<sub>3</sub>N<sub>5</sub>/BN.

In summary, a Ta<sub>3</sub>N<sub>5</sub>/BN composite photocatalyst is synthesized via the NH<sub>4</sub>Cl-based vacuum nitridation process. The Ta<sub>3</sub>N<sub>5</sub> component exhibits highly crystallized nanorod morphology during growth on the BN substrate. Photodeposition of Ag metal, chemical state analysis and carrier dynamics assessment confirmed electron transfer between Ta<sub>3</sub>N<sub>5</sub> and BN. Enhanced photocatalytic performance in water splitting emphasizes the promotion of the charge separation efficiency by electron interaction at the catalyst/substrate interface. Our work not only provides a new method for synthesizing highly crystallized Ta<sub>3</sub>N<sub>5</sub> nanorods but also demonstrates an efficient composite structure for enhancing the photocatalytic performance of this promising photocatalyst.

This work was financially supported by the National Natural Science Foundation of China (22572123), Shanghai Natural Science Foundation of China (24ZR1451400), Starting Foundation of ShanghaiTech University, and Double First-Class Initiative Fund of ShanghaiTech University. J. F. Zhang acknowledges financial support from the Shanghai Rising-Star Program (Yangfan Special Project, 24YF2729000), and the Science and Technology Commission of Shanghai Municipality (STCSM). We also acknowledge the support from Analytical

Instrumentation Center (no. SPST-AIC10112914) and CħEM (no. EM02161943), SPST of ShanghaiTech University.

#### Conflicts of interest

There are no conflicts to declare.

### Data availability

The data supporting this article have been included as part of the supplementary information (SI). Supplementary information is available. The detailed SEM images, XPS spectra, experiment conditions were displayed in supplementary information. See DOI: https://doi.org/10.1039/d5cc03833b.

#### Notes and references

- 1 W. Wang, X. Xu, W. Zhou and Z. Shao, Adv. Sci., 2017, 4, 1600371.
- 2 Q. Yang, X. Tong and Z. Wang, Mater. Rep.: Energy, 2024, 4, 100253.
- 3 Q. Wang and K. Domen, Chem. Rev., 2020, 120, 919-985.
- 4 Q. Wang, C. Pornrungroj, S. Linley and E. Reisner, Nat. Energy, 2021, 7, 13-24.
- 5 S. Ye, W. Shi, Y. Liu, D. Li, H. Yin, H. Chi, Y. Luo, N. Ta, F. Fan and X. Wang, et al., J. Am. Chem. Soc., 2021, 143, 12499-12508.
- 6 M. S. Prévot and K. Sivula, J. Phys. Chem. C, 2013, 117, 17879-17893. 7 J. H. Kim, J. W. Jang, Y. H. Jo, F. F. Abdi, Y. H. Lee, R. van de Krol
- and J. S. Lee, Nat. Commun., 2016, 7, 13380. 8 L. Pan, J. H. Kim, M. T. Mayer, M.-K. Son, A. Ummadisingu, J. S. Lee,
- A. Hagfeldt, J. Luo and M. Grätzel, Nat. Catal., 2018, 1, 412-420.
- 9 Z. Wang, Y. Inoue, T. Hisatomi, R. Ishikawa, Q. Wang, T. Takata, S. Chen, N. Shibata, Y. Ikuhara and K. Domen, Nat. Catal., 2018, 1, 756–763.
- 10 Y. Q. Xiao, C. Feng, J. Fu, F. Z. Wang, C. L. Li, V. F. Kunzelmann, C. M. Jiang, M. Nakabayashi, N. Shibata and I. D. Sharp, et al., Nat. Catal., 2020, 3, 932-940.
- 11 G. Hitoki, A. Ishikawa, T. Takata, J. N. Kondo, M. Hara and K. Domen, Chem. Lett., 2002, 736-737.
- 12 G. Fan, T. Fang, X. Wang, Y. Zhu, H. Fu, J. Feng, Z. Li and Z. Zou, iScience, 2019, 13, 432-439.
- 13 J. Fu, F. Wang, Y. Xiao, Y. Yao, C. Feng, L. Chang, C.-M. Jiang, V. F. Kunzelmann, Z. M. Wang and A. O. Govorov, et al., ACS Catal., 2020, 10, 10316-10324.
- 14 S. S. Ma, T. Hisatomi, K. Maeda, Y. Moriya and K. Domen, J. Am. Chem. Soc., 2012, 134, 19993-19996.
- 15 K. N. Sun, Y. Y. Li, Q. G. Zhang, L. Wanga, J. L. Zhang and X. Zhou, Appl. Surf. Sci., 2017, 405, 289-297.
- 16 X. Wang, H. Huang, G. Fan, Z. Li and Z. Zou, J. Phys. Chem. C, 2017, 122, 489-494.
- 17 M. Xiao, S. C. Wang, S. Thaweesak, B. Luo and L. Z. Wang, Engineering, 2017, 3, 365-378.
- 18 D. Wang, T. Hisatomi, T. Takata, C. Pan, M. Katayama, J. Kubota and K. Domen, Angew. Chem., Int. Ed., 2013, 52, 11252-11256.
- 19 Y. Xiang, B. Zhang, J. Liu, S. Chen, T. Hisatomi, K. Domen and G. Ma, Chem. Commun., 2020, 56, 11843-11846.
- 20 Y. Xu, K. Liu, J. Zhang, B. Zhang, J. Zhang, K. Shi, H. Wang and
- G. Ma, J. Energy Chem., 2024, 94, 541-550. 21 K. Liu, B. Zhang, J. Zhang, W. Lin, J. Wang, Y. Xu, Y. Xiang, T. Hisatomi, K. Domen and G. Ma, ACS Catal., 2022, 14637-14646,
- DOI: 10.1021/acscatal.2c04361. 22 K. Liu, B. Zhang, J. Zhang, Y. Xu, J. Zhang, Z. Zhang, K. Shi, N. Wang, S. Chen and G. Ma, ACS Catal., 2024, 14, 10138-10147.
- 23 D. L. Lu, M. Hara, T. Hisatomi, T. Takata and K. Domen, J. Phys. Chem. C, 2009, 113, 17151-17155.
- M. Li, W. Luo, D. Cao, X. Zhao, Z. Li, T. Yu and Z. Zou, Angew. Chem., Int. Ed., 2013, 52, 11016-11020.